University of Birmingham

Research at Birmingham

MIMO array for short-range, high-resolution automotive sensing

Sayin, Alp; Pooni, Sukhjit; Hoare, Edward; Antoniou, Michail

[Link to publication on Research at Birmingham portal](#)

IET Radar, Sonar & Navigation

MIMO Array for Short-Range, High-Resolution Automotive Sensing

MIMO Array for Short-Range, High-Resolution Automotive Sensing

Alp Sayin[1], Sukhjit Pooni[1], Edward Hoare[1], Michael Antoniou[1*]

[1]Department of Electronic, Electrical and Systems Engineering, University of Birmingham, Birmingham, United Kingdom
[*]m.antoniou@bham.ac.uk

The paper introduces the concept of Multiple Input-Multiple Output (MIMO) radar or sonar arrays for short-range, high-resolution sensing in vehicular applications. The use of a MIMO architecture, which is becoming increasingly popular in this field, is selected to reduce the amount of physical elements in the array needed for beamforming, but also to allow signal processing approaches for forming narrow beams in the near-field of the array. The paper analytically derives the proposed signal processing approach, and then verifies it via simulated and experimental data in a laboratory environment with scientific equipment assembled for this purpose.

1. Introduction

A number of radar and sonar sensors are used onboard vehicles for a suite of applications. One of the most common types of sensors are radar phased arrays, now operating in a dedicated frequency band (~76 GHz), with a traditional use in mid- and long-range applications such as cruise control, for example.

As the number of autonomous features in vehicles increases, so does the need for additional radar/sonar sensors and/or sensing capabilities. One of the emerging areas in this field is the monitoring of areas at short ranges (typically a few metres) from the vehicle. Rather than just detecting the presence of an object in the vicinity of a vehicle (e.g. blind spot detection or proximity sensing), it may be beneficial to also pinpoint its exact location in range and angle, or even identify its speed and track it if it is moving, so the vehicle can then make a more informed decision on possible actions such as emergency breaking or steering. These properties would make such system attractive for numerous automotive applications in an urban environment, including parking aids, emergency braking, blind spot detection, speed-over-ground estimation etc. However, the caveat to be addressed is that such capabilities require sensor arrays to form beams in their near-field.

This paper brings forward the concept of using linear, MIMO sensor arrays for short-range, high-resolution automotive sensing. The sensors themselves could be RF or ultrasonic, however since in our experimentation we have considered radar sensors only we will limit this discussion to RF. MIMO radar has already been proposed for medium-/far-range automotive applications[1]–[12], and in fact there are commercial chipsets available on the market[13], [14], so the same instruments could be used for short-range sensing with the appropriate signal processing. One of their main benefits is the fact that they form beams through signal processing, rather than physical space, and through their "virtual" array concept they can allow a MIMO array of N transmit + M receive physical elements to form the same beam patterns (geometrically) as an NxM phased array, which reduces system costs. Furthermore, since MIMO arrays scan digitally rather than physically, they can persistently monitor the whole area in their field of view.

MIMO arrays are additionally considered as a technology enabler for the range of applications mentioned above because since they form beams at the signal processing level, it may be possible to derive signal processing algorithms to perform near-field corrections and therefore form narrow beams at stand-offs in the order of a few metres, which would not be possible for phased arrays of similar dimensions. Near-field MIMO has been considered for two-dimensional, high-resolution imaging applications, but the array configuration and the very task at hand are substantially different to those of a vehicular, linear MIMO radar[15], [16]. Therefore, the appropriate feasibility study is needed.

This paper considers the problem of forming beams with a MIMO array in the near-field of the sensor, as an enabler for automotive applications requiring short-range and high angular resolution. The general approach was to derive element phase differences for an arbitrary MIMO array in near-field. Then, using the exact element phase differences, digital focusing of MIMO near-field beam patterns was performed using the far-field approximated element phase differences as the basis. Signal processing algorithms to do so are analytically derived, and then tested using both simulated and proof-of-concept experimental data obtained in laboratory conditions (an anechoic chamber) with scientific equipment. At the time of experimentation commercial MIMO devices at the automotive frequency band were not available in our laboratory, however the methods and results reported here are not frequency-dependent. The rest of the paper is organised as follows: Section 2 provides analytical results on MIMO array beamforming in the far-field (for reference) and derives the near-field algorithm. Section 3 describes the experimental setup, while Section 4 presents and discusses experimental results obtained in comparison with simulation results mimicking the experimental setup.

2. MIMO Array

2.1. Beamforming in Far-field

The linear MIMO array considered here comprises separate transmit and receive sub-arrays. Transmit elements emit "orthogonal" waveforms, i.e. signals with low cross-correlation values. In practice, to provide such waveforms is a formidable task, but as this study focuses on near-field beam formation this problem falls outside its scope. The directivity

1

pattern of a sensor array with respect to transmit and/or receive angle is often referred to as the array factor, which is the summation of complex contributions from its elements assumed they're isotropic[17, p. 53]. The product of array factor and element pattern can then be used to produce the array pattern[18, p. 7]. And the MIMO array-factor can then be written as the multiplication of transmit and receive array factors[19].

For the clarification of variables and signals a sketch of a 4x4 MIMO array has been given in Fig. 1 with parametric variables. We start with the geometry of a MIMO array with uniform linear sub-arrays and beamforming in far-field.
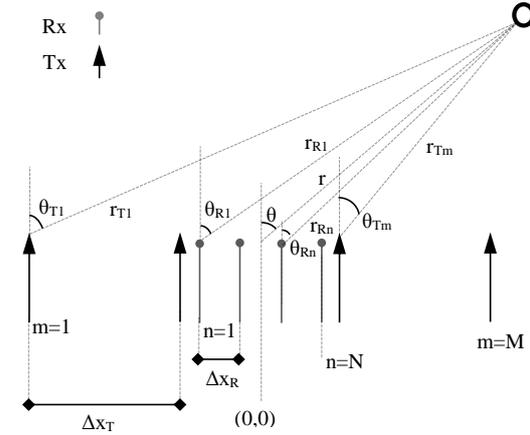

Fig. 1 *MIMO array geometry*

In Fig. 1 and in the following equations; θ represents the azimuth angle from the array centre to the target. Respectively, θ_{Tm} and θ_{Rn} represent the individual angles from transmit and receive array elements. M and N represents the total number of transmit and total number of receive elements. Similarly m and n are indices that are used for representing transmit and receive elements. Range r represents the range from the physical centre of the array to the target. Respectively, r_{Tm} and r_{Rn} represent the individual ranges from transmit and receive array elements.   The distances Δx_t and Δx_r represent the transmit sub-array element spacing and receive sub-array spacing respectively. It is assumed that the physical centres of the sub-arrays are at the same position.

If far-field approximations were to be applied, then all angles from all elements to an arbitrary target could be taken as approximately equal:

$$\theta_{Tm} = \theta_{Rn} = \theta \ \forall \ m = [1 \dots M] \ \& \ n = [1 \dots N] \tag{1}$$

Then r_{Tm} and r_{Rn} can be written as [20]:

$$r_{Rn} = r + \left(\frac{N-1}{2} - (n-1)\right) \cdot \Delta x_R \cdot sin(\theta) \tag{2}$$

$$r_{Tm} = r + \left(\frac{M-1}{2} - (m-1)\right) \cdot \Delta x_T \cdot sin(\theta) \tag{3}$$

In a far-field scenario, a coarse sub-array can be used with a fine sub-array to cancel out grating lobes of the coarse array with the fine array's null locations to yield a Sinc-like pattern[19]. After matched filtering, sum of received signals can be written as:

$$s_r(t) = s_{MF}(t - \tau) \cdot \sum_{n=1}^{N} e^{-jkr_{Rn}} \cdot \sum_{m=1}^{M} e^{-jkr_{Tm}} \tag{4}$$

where τ is the time delay from transmitter to target and back to receiver. From (4), MIMO array factor can be written as:

$$AF_{mimo}(r,\theta) = \sum_{n=1}^{N} e^{-jkr_{Rn}} \cdot \sum_{m=1}^{M} e^{-jkr_{Tm}} \tag{5}$$

And since each summation is the array factor of the corresponding sub-array [21], the MIMO array factor can then be written as the multiplication of transmit and receive array factors as:

$$AF_{mimo}(r,\theta) = AF_{Rx}(r_{Rn},\theta) \cdot AF_{Tx}(r_{Tm},\theta) \tag{6}$$

where $AF_{Rx}(\theta)$ is the array factor of receiver sub-array, and $AF_{Tx}(\theta)$ is the array factor of transmitter sub-array. As can be observed from this derivation, the fact that MIMO array factor is the product of its sub-array factors is independent of the range r as the derivation did not require the substitution of ranges r_{Rn} and r_{Tm} with the far-field approximated ranges given in (2) and (3).

If the approximations are applied, the MIMO array factor approximates to a Sinc function independent of the r, given that r satisfies the conditions for the far-field. However, this is only explained here as a reference, and is not in the scope of this paper and will not be discussed any further.

It can also be seen that MIMO array factor is the sum of $M \times N$ phase shifts, where each of the m and n combination represents a virtual element signal. Hence, MIMO array factor can also be represented as a single array factor of its virtual array as:

$$AF_{mimo}(r,\theta) = \sum_{p=1}^{M*N} e^{-jk(r_{T(p \, mod \, M)}+r_{R(\lceil p/N \rceil)})} \tag{7}$$

For all signal processing purposes, necessary complex weights can be applied separately in the data-path for each element. Any processing can also be applied at a sub-array level, so a MIMO array can be steered to an arbitrary angle using separate transmit and receive steering[22]. These would be the same steering methods for a uniform linear phased array [21]. Performing this processing for all angles of interests yields a reflection intensity map as a function of range and angle (see Fig. 2).

2.2. MIMO Array Factor in Near-field

In the near-field, the approximations that lead the array factor into a Sinc-like pattern fail and therefore beamforming independent of range yields undesirable patterns as will be shown in the next section. As shown before, the MIMO array

2

factor is still the multiplication of the array factors of transmit and receive array, because this phenomenon is based on signal orthogonality rather than geometry. Therefore, this derivation can then substituted in MIMO array factor; both for transmit sub-array and receive sub-array factors to yield near-field MIMO array factor. The geometry assumed is the same as in Fig. 1.
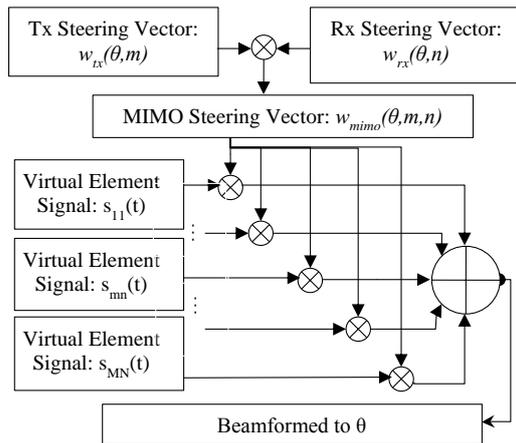

Fig. 2 *Block diagram for MIMO beamformer at far-field*

The angle θ_{Rn} can be written as:

$$\theta_{Rn} = \text{atan}\left(\frac{r * sin(\theta) + \left(\frac{N - 2n + 1}{2}\right)\Delta x_R}{r \cdot \cos(\theta)}\right) \qquad (8)$$

Since all elements are assumed to share the same range in Y dimension, from the cosine of r_{Rn}, it can be written as:

$$r_{Rn} = \frac{r \cdot \cos(\theta)}{\cos(\theta_{Rn})} \qquad (9)$$

Then (8) can be used to substitute θ_{Rn} into (9) to obtain a definition of r_{Rn}:

$$r_{Rn} = \left(r^2 + \sin(\theta)\,(N - 2n + 1)\Delta x_R \right. $$
$$\left. + \frac{(N - 2n + 1)^2(\Delta x_R)^2}{4}\right)^{\frac{1}{2}} \qquad (10)$$

Using the exact range r_{Rn}, it is now possible to numerically compute the beam patterns at various ranges. Since the transmit and receive arrays are linear arrays, the computation of exact ranges to a target from transmit array elements can be written using (20) as:

$$r_{Tm} = \left(r^2 + \sin(\theta)\,(M - 2m + 1)\Delta x_T \right. $$
$$\left. + \frac{(M - 2m + 1)^2(\Delta x_T)^2}{4}\right)^{\frac{1}{2}} \qquad (11)$$

Regardless of the near-field condition, signal model can still be written as (4) therefore still allowing the MIMO array factor to be represented as the multiplication of individual sub-array factors as in (5). Substituting (10) and (11) in (5) would yield the array factor in near-field.

2.3. Near-Field Focusing Technique

The beam pattern can be adjusted via means of digital beamforming techniques. The most obvious technique would be to use a back-projection algorithm to avoid nearfield effects, however a back-projection algorithm is mostly used for imaging and is already known to be computationally intensive[23]. Some other techniques -which are similar to beam steering in nature- are simply applying complex weights to received signals to shift the received phases to far-field phases. These techniques are known and already used for near-field focusing for phased arrays. Examples and variations of these techniques can be found in literature. The method of having an extra set of complex weights (other than beam steering weights) has been proposed in to obtain a desired far field beam pattern [2]. It's proposed that these weights can shift the received phases to an arbitrary far range phase where one can obtain a desirable beam pattern [24]. Kennedy et al. also suggested using the ideal far-field phases to generate the most ideal beam pattern possible in another study[25].

The approach here is to use these methods in conjunction with MIMO array theory. For the sake of simplicity, the near-field focusing method will be first derived for receive sub-array.

A focusing method based on the differences of ideal far-field phases and near-field phases can be defined such that the sum of received phases and phases of this function would yield ideal far-field phases. Normally, this function would depend on r_{Rn}, which can be written in form of r, θ, n and dR and since N and dR are constants for a given array, this function can be written as a function of r, θ, n as:

$$g_{rx}(\theta, n, r) \cdot e^{-jkr_{Rn}} = e^{-jkr_{nfar}} \qquad (12)$$

Where g_{rx} stands for the phase correction function and r_{nfar} stands for a range in far-field where ideal patterns are obtained. This function can be inserted into the array factor as the near-field focusing weights as:

$$AF_{rx}(r, \theta) = \sum_{n=1}^{N} g_{rx}(\theta, n, r) \cdot e^{-jkr_{Rn}} \qquad (13)$$

Once the far-field phases are artificially obtained functions that rely on far-field beam patterns can be used as is (e.g. conventional beam steering weights for digital steering). The phase shifts needed can be computed using the difference between the real phase shift and the ideal phase shift by using (10) and (2) as:

$$r_{Rn} - r_{Rnfar} = \left(r^2 + \Delta x_R \sin(\theta)\,(N - 2n + 1) \right. $$
$$\left. + \frac{(N - 2n + 1)^2(\Delta x_R)^2}{4}\right)^{\frac{1}{2}} - r \qquad (14)$$
$$+ \left(\frac{N - 2n + 1}{2}\right)\Delta x_R sin(\theta)$$

Similarly, a function like that can be defined for the transmit array too as:

3

$$g_{tx}(\theta, m, r) = e^{jk(r_{Tm} - r_{Tmfar})} \tag{15}$$

Since the transmit and receive arrays share similar geometry and variables, nearfield correction function for the transmit array can be written by rearranging (14) as:

$$
\begin{aligned}
r_{Tm} - r_{Tmfar} = & \left(r^2 + \Delta x_T \sin(\theta) \, (M - 2m + 1) \right. \\
& \left. + \frac{(M - 2m + 1)^2 (\Delta x_T)^2}{4} \right)^{\frac{1}{2}} - r \\
& + \left(\frac{M - 2m + 1}{2} \right) \Delta x_T \sin(\theta)
\end{aligned}
\tag{16}
$$

Shifting the phases this way is like digitally adjusting the locations of the array elements such that they would look like a lens. This process is range- and angle-dependent therefore needs to be applied to all range-angle pairs, however it requires no knowledge of actual target positions for corrections. This computation can be easily done for all range-angle pairs of interest. And by defining a separate function for receive and transmit sub-arrays, number of computations is minimised compared to applying this method to the virtual array.

With the near-field focusing, the MIMO array factor now takes the formulation as:

$$
\begin{aligned}
AF_{mimo}(r, \theta) \\
= \left(\sum_{n=1}^{N} (w_{rx}(\theta, n) g_{rx}(\theta, n, r) e^{jk r_{Rn}}) \right) \\
\cdot \left(\sum_{m=1}^{M} (w_{tx}(\theta, m) g_{tx}(\theta, m, r) e^{jk r_{Tm}}) \right)
\end{aligned}
\tag{17}
$$

After the insertion of near-field phase corrections, the new system block diagram can be seen in
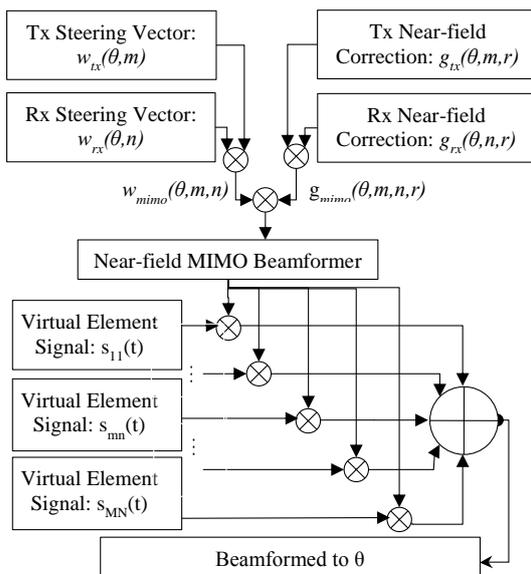Fig. **3**.

Fig. **3** Block diagram for MIMO beamformer at near-field

In Fig. 4 the beam pattern at 10λ range with 3x5 MIMO array without near-field focusing can be seen, accompanied by the beam pattern an equivalent 15-element phased array would yield. Sidelobe levels are as high as the main lobe level, and the directive gain loss is approximately 5dB. The beam pattern at 10λ range with near-field focusing can be seen as it has the shape of an almost perfect Sinc function apart from the relatively higher sidelobes outside of -65 and 65°. The ideal far-field beam pattern can be seen as a Sinc function as obtained previously via computations. The ideal far-field beam pattern makes it easier to observe the difference of relatively higher sidelobe levels in near-field focused beam pattern. However, this slight increase in sidelobe levels are negligible since the level is still under the first sidelobe level of -13dB.
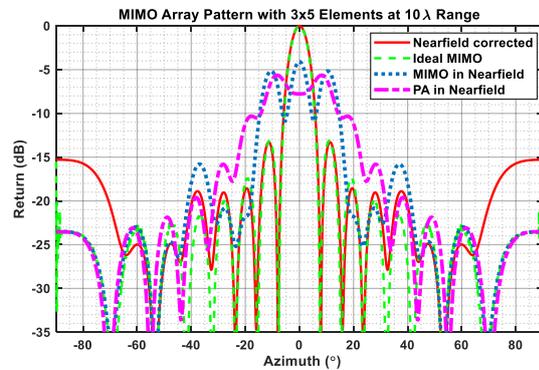
Fig. 4 Computed near-field beam-patterns with and without near-field focusing compared to an ideal far-field pattern

3. Simulations & Experiments

A MIMO radar simulator has been coded to confirm the proposed approach alongside laboratory experiment environment. The simulation programme works with point targets in 3-dimensional coordinate space. Simulation parameters are similar to those of our experimental setup and can be found in Table 1.

In experimental system, a Time Division Multiple Access (TDMA) MIMO setup has been implemented, which is similar to that of commercial devices. This was used throughout the experimentation process, to circumvent limitations of experimental equipment, including simultaneous signal transmission over multiple channels, relatively low receiver dynamic range, and sample rate requirements, but more importantly so that near-field algorithms can be tested without the presence of these artefacts. And also TDMA is the scheme used by current commercial systems.

The first set of experiments were performed with existing equipment to test our theory and algorithms and to verify our simulations. To generate compressed waveforms a Tektronix AWG7102 arbitrary waveform generator was used. And to capture the reflected signals, a Tektronix DPO72004C digital phosphorus oscilloscope was used. The captured signals were then transferred to MATLAB in a desktop computer for

4

processing. In order to overcome the required number of signal capture channels, signals were downconverted to a low-IF band and then recorded with DPO. For the purposes of downconverting a HP-8648D RF signal generator was used. The recorded low-IF signals were then downconverted again to baseband digitally in MATLAB. Transmission of the signals were done via directional horn antennas. Receive antennas were custom design low-gain antennas built in our laboratory. A Gaussian window was applied to transmit waveform to avoid range sidelobes. A system block diagram summarising the setup can be seen in Fig. 5. And the final experiment parameters can be seen below in Table 1.
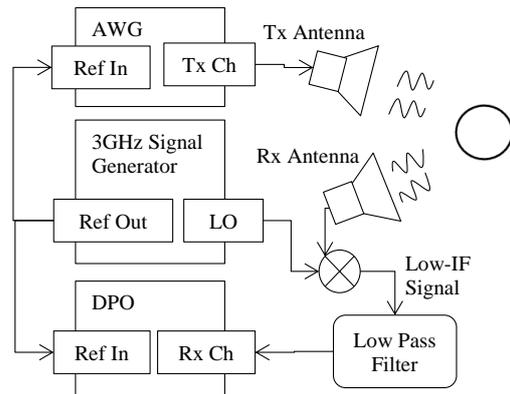

Fig. 5 *Experimental system hardware block diagram*

Table 1 Experiment Parameters

Property	Value	Unit
Number of Tx	3	-
Number of Rx	5	-
Carrier Frequency	3.5	GHz
Waveform	Upchirp LFM	-
Multiple Access Scheme	TDMA	-
Bandwidth	1 Ghz	GHz
Range Window	Gaussian	-
Tx Antenna Gain	8	dBi
Tx Antenna Beamwidth	60	degrees
Tx Power Out	25	dBm
Rx Antenna Gain	2	dBi
Rx Antenna Beamwidth	120	degrees
Receive Gain	24.5	dB
Tx Element Spacing	20	cm
Rx Element Spacing	4	cm
Sample Rate	3.125	GHz
Number of Pulses	500	-
Pulse Length	2	us
PRI	1	ms

Experimental scenarios were designed to prove beamforming capabilities at various angles and –near-field-ranges. Prior to measurements with targets, recordings with the empty anechoic chamber were made and processed to form the corresponding range/angle maps. Those were then subtracted from any recording with a target, which allowed compressed echoes from the chamber itself and direct signal

artefacts to be suppressed, hence allowing for a better assessment of beamforming performance.

3.1. Scenarios

Various experiments were performed where a target was placed about 1.2m away from the radar and at about 0° and 25° azimuth angles, to identify the angular range over which the MIMO array can perform.

In Fig. 6 are the photos of the 2 scenarios that are used for experiments with a 3x5 MIMO radar. The scenarios are presented as photos from-the-top taken inside the anechoic chamber during the experiments.
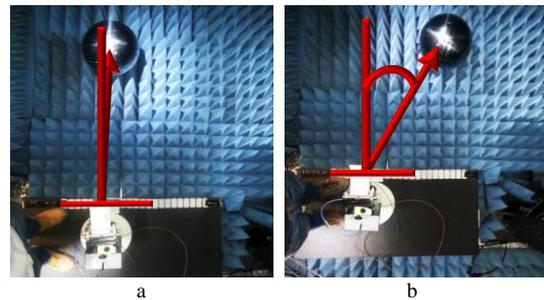

Fig. 6 *Experiment scenarios*
(a) Target at 0°, (b) Target at 25°

3.2. Results and Discussion

Below, the results from experiments are presented with their corresponding simulations. For each scenario; first, the experimental and simulation results without near-field corrections are compared and then same results with near-field corrections are shown and compared. All colour plots share the same dynamic range which is from -25dB to 0dB, where each colour plot is normalised to its own maximum. All colour plots also share the same Y-axis which covers ranges from 0.85m to 2m, and all plots including azimuth cuts share the same X-axis which covers angles from -90° to +90°. Sidelobe and beamwidth measurements from results with target at 0° can be found in Table 2, and measurements from results with target at 25° can be found in

Table **3**.

Single Target at 0°: In Fig. 7a the simulated range-angle map of a target at about 0° with a MIMO array without near-field focusing, accompanied with its azimuth cut in Fig. 7b at the target range. The target can be located at 0° and at 1.15 metres, but alongside it can be observed relatively high sidelobe levels. The high sidelobe level is not an indicator of anything since first nulls of the beam pattern are not low enough. The shape of the sidelobe structure is as expected from a MIMO array operating at this range; structure shows a decreasing pattern as it gets further from the target, but presence of high first sidelobe levels are observed because of failure in beamforming at such short ranges. In Fig. 7c is the experimentally acquired range-angle map of a target at ~0° with a MIMO array without near-field focusing, accompanied with its azimuth cut in Fig. 7d at the target range. The target can be located at 0° and at ~1.15 metres. The beam structure

5

at this range is very similar to the simulated result with minor differences.

Fig. 7 *Target at 0° without near-field corrections*
(a) Simulation, (b) Azimuth cut of simulation,
(c) Experiment, (d) Azimuth cut of experiment

In Fig. 8a the simulated range-angle map of a target at 0.5° with a MIMO array with near-field focusing, accompanied with its azimuth cut in Fig. 8b at the target range. The target can be located at 0° and at 1.15 metres. The beam structure at this range is not distorted and looks like a Sinc function one would obtain at far-field. This simulation clearly demonstrates the effect of near-field focusing in such close ranges. Also in Fig. 8c is the experimentally acquired range-angle map of a target at ~0° with a MIMO array with near-field focusing, accompanied with its azimuth cut in Fig. 8d at the target range. The target can be located at 0° and at 1.15 metres. The beam structure at this range is very similar to the simulated result with minor differences such as some asymmetry in the sidelobes.
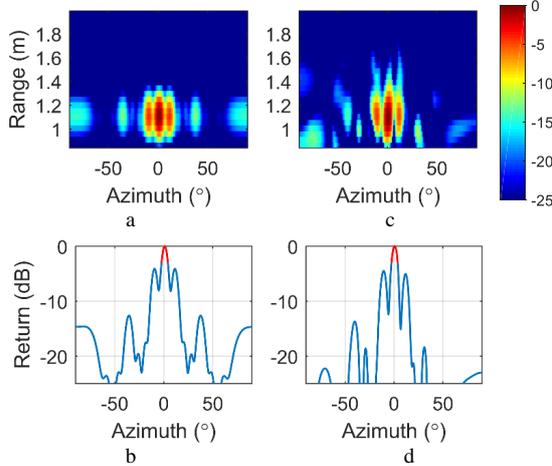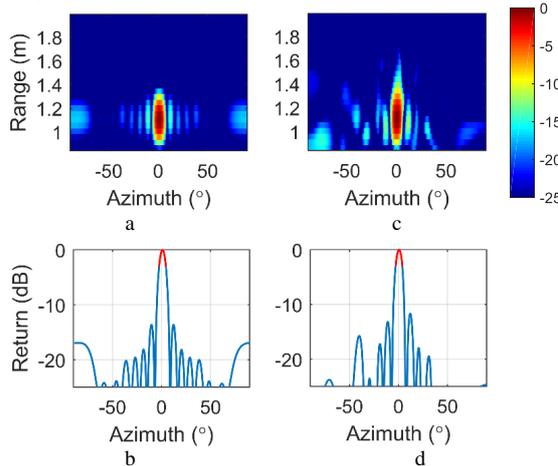

Fig. 8 *Target at 0° with near-field corrections*

(a) Simulation, (b) Azimuth cut of simulation,
(c) Experiment, (d) Azimuth cut of experiment

Table 2 *Target at 0 degrees; simulation and experimental sidelobe and beamwidth measurements with and without near-field corrections*[1]

Target at 0°	Sidelobe	Beamwidth
Sim. wo/ Cor	-4.09 dB	6.46°
Exp. wo/ Cor	-4.48 dB	6.30°
Sim. w/ Cor	-13.63 dB	6.92°
Exp. w/ Cor	-11.67 dB	6.83°
Expected	-13.1 dB	7.15°

Single Target at 25°: In Fig. 9a the simulated range-angle map of a target at 25° with a MIMO array without near-field focusing, accompanied with its azimuth cut in Fig. 9b at the target range. The target can be located at ~23.5° and at 1.10 metres, which is 1 degree off compared to the simulation scenario. Alongside the main lobe are again relatively high sidelobe levels.

In Fig. 9c is the experimentally acquired range-angle map of a target at ~25° with a MIMO array without near-field focusing, accompanied with its azimuth cut in Fig. 9d at the target range. The target can be located at 23.5° and at 1.15 metres.
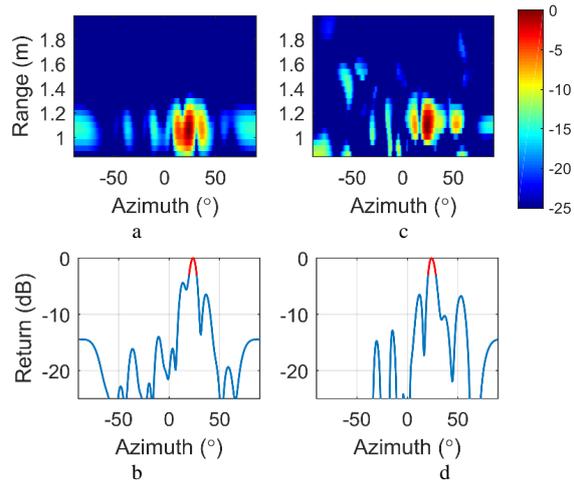

Fig. 9 *Target at 25° without near-field corrections.*
(a) Simulation, (b) Azimuth cut of simulation,
(c) Experiment, (d) Azimuth cut of experiment

In Fig. 10a the simulated range-angle map of a target at 25° with a MIMO array with near-field focusing, accompanied with its azimuth cut in Fig. 10b at the target range. The target can be located at 24.5° and at 1.10 metres. The beam structure at this range resembles a Sinc function. This simulation also shows the effect of near-field focusing in such close ranges.

In Fig. 10c is the experimentally acquired range-angle map of a target at ~25° with a MIMO array with near-field focusing, accompanied with its azimuth cut in Fig. 10d at the target range. The target can be located at 23.5° and at 1.15

6

---

[1] Sim wo/ Cor stands for Simulation without near-field corrections. Similarly Exp w/ Cor stands for Experiment with near-field corrections.

metres. The shape of the sidelobe structure is not identical to a Sinc function. However, the 3-dB beamwidth match simulation results while some returns from the chamber are still visible (e.g. returns at close ranges and negative angles) and hence could be interfering with the response of the target.
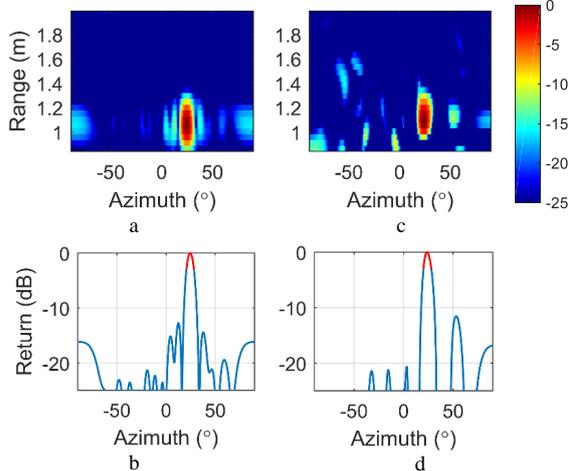

Fig. 10 *Target at 25° with near-field corrections.*
(a) Simulation, (b) Azimuth cut of simulation,
(c) Experiment, (d) Azimuth cut of experiment

Table 3 *Target at 25 degrees; simulation and experimental sidelobe and beamwidth measurements with and without near-field corrections*

Target at 25°	Sidelobe	Beamwidth
Sim. wo/ Cor	n/a	7.57°
Exp. wo/ Cor	n/a	8.71°
Sim. w/ Cor	-12.73 dB	7.66°
Exp. w/ Cor	-11.54 dB	7.95°
Expected	-13.1 dB	7.85°

Overall, it can be said that there is good correspondence between all experimental results and simulations results.

4. Conclusions and Future Work

During this research, the fundamental theory of near-field MIMO radar for beamforming at short ranges has been investigated.

Existing methods of near-field focusing for phased arrays have been studied. These methods then were used to develop MIMO near-field focusing methods, and they have been computationally verified at various ranges to observe focusing effects.

MIMO near-field array factor computations and beamforming algorithms have been coded in MATLAB. In addition, a simulation program was written to simulate MIMO arrays for comparison of simulation and experimental results in near-field.

A hardware setup was built for performing trials in a controlled environment to verify experimental near-field beamforming capabilities using a MIMO radar setup. These experiments included scenarios containing a single target at near-field ranges and various angles to verify near-field

focusing capabilities and to confirm expected performance such as 3-dB beamwidth and first-sidelobe level.

All experimental scenarios were simulated using the MIMO simulation programmes for comparison of experimental results, and for proof of improvement. It was found that the near-field MIMO array beamforming works well within expected parameters in a controlled environment, and that the experimental results match simulation results within nominal deviations up to a scan angle of 25°. It was also confirmed that a near-field focused MIMO can perform significantly better than a non-near-field-focused MIMO. The obtained results confirm our understanding of near-field MIMO radar theory and the feasibility of our approach for employing MIMO radars for automotive sensing purposes.

The next stage in the pursuit of this research is to transit from experimental proof-of-concept in laboratory conditions with a commercial MIMO radar, under real conditions where practical problems such as direct signal suppression can be considered, and where the performance of the system from the point of view of specific applications can be assessed.

5. Acknowledgements

6. References

[1]   Y. L. Sit, T. T. Nguyen, C. Sturm, and T. Zwick, '2D radar imaging with velocity estimation using a MIMO OFDM-based radar for automotive applications', in Radar Conference (EuRAD), 2013 European, 2013, pp. 145–148.

[2]   K. Iwasa, T. Kishigami, H. Yomo, A. Matsuoka, and J. Satou, 'MIMO radar system using orthogonal complementary codes with Doppler offset', in 2017 European Radar Conference (EURAD), 2017, pp. 102–105.

[3]   M. Harter, J. Hildebrandt, A. Ziroff, and T. Zwick, 'Self-Calibration of a 3-D-Digital Beamforming Radar System for Automotive Applications With Installation Behind Automotive Covers', IEEE Transactions on Microwave Theory and Techniques, vol. 64, no. 9, pp. 2994–3000, Sep. 2016 [Online]. Available: http://ieeexplore.ieee.org/document/7536163/. [Accessed: 05-Mar-2018]

[4]   D. Guermandi et al., 'A 79-GHz 2 $\times$ 2 MIMO PMCW Radar SoC in 28-nm CMOS', IEEE Journal of Solid-State Circuits, vol. 52, no. 10, pp. 2613–2626, Oct. 2017 [Online]. Available: http://ieeexplore.ieee.org/document/7997699/. [Accessed: 05-Mar-2018]

[5]   C. Vasanelli, R. Batra, A. D. Serio, F. Boegelsack, and C. Waldschmidt, 'Assessment of a Millimeter-Wave Antenna System for MIMO Radar

7

Applications', IEEE Antennas and Wireless Propagation Letters, vol. 16, pp. 1261–1264, 2017 [Online]. Available: http://ieeexplore.ieee.org/document/7752791/. [Accessed: 05-Mar-2018]

[6]   F. Engels, M. Wintermantel, and P. Heidenreich, 'Automotive MIMO Radar Angle Estimation in the Presence of Multipath'.

[7]   P. Khomchuk, I. Stainvas, and I. Bilik, 'Pedestrian motion direction estimation using simulated automotive MIMO radar', IEEE Transactions on Aerospace and Electronic Systems, vol. 52, no. 3, pp. 1132–1145, Jun. 2016 [Online]. Available: http://ieeexplore.ieee.org/document/7511847/. [Accessed: 05-Mar-2018]

[8]   A. Sommer, T. T. Ngo, and J. Ostermann, '3D multiple input single output near field automotive synthetic aperture radar', in Radar Symposium (IRS), 2017 18th International, 2017, pp. 1–10.

[9]   C. Vasanelli, R. Batra, and C. Waldschmidt, 'Optimization of a MIMO radar antenna system for automotive applications', in Antennas and Propagation (EUCAP), 2017 11th European Conference on, 2017, pp. 1113–1117.

[10]   P. Swami, A. Jain, P. Goswami, K. Chitnis, A. Dubey, and P. Chaudhari, 'High performance automotive radar signal processing on TI's TDA3X platform', in Radar Conference (RadarConf), 2017 IEEE, 2017, pp. 1317–1320.

[11]   C. Pfeffer, R. Feger, C. Wagner, and A. Stelzer, 'FMCW MIMO Radar System for Frequency-Division Multiple TX-Beamforming', IEEE Transactions on Microwave Theory and Techniques, vol. 61, no. 12, pp. 4262–4274, Dec. 2013 [Online]. Available: http://ieeexplore.ieee.org/document/6670120/. [Accessed: 05-Mar-2018]

[12]   R. Feger, C. Pfeffer, and A. Stelzer, 'A Frequency-Division MIMO FMCW Radar System Based on Delta–Sigma Modulated Transmitters', IEEE Transactions on Microwave Theory and Techniques, vol. 62, no. 12, pp. 3572–3581, Dec. 2014 [Online]. Available: http://ieeexplore.ieee.org/lpdocs/epic03/wrapper.htm?arnumber=6937213. [Accessed: 05-Mar-2018]

[13]   'TEF810X Fully-Integrated 77 GHz Radar Transceiver|NXP'. [Online]. Available: https://www.nxp.com/products/rf/radar-transceivers/tef810x-fully-integrated-77-ghz-radar-transceiver:TEF810X. [Accessed: 26-Feb-2018]

[14]   'AWR1642 Single-Chip 76-to-81GHz Automotive Radar Sensor Integrating DSP and MCU | TI.com'. [Online]. Available: http://www.ti.com/product/AWR1642. [Accessed: 26-Feb-2018]

[15]   Y. Zhen, L. Wei, C. Qinggong, and H. Dahai, 'Design of a near-field radar imaging system based on MIMO array', in Electronic Measurement & Instruments (ICEMI), 2015 12th IEEE International Conference on, 2015, vol. 3, pp. 1265–1269 [Online]. Available: http://ieeexplore.ieee.org/abstract/document/7494513/. [Accessed: 04-Sep-2017]

[16]   T. Spreng, U. Prechtel, B. Schonlinner, V. Ziegler, A. Meusling, and U. Siart, 'UWB near-field MIMO radar: Calibration, measurements and image reconstruction', in Radar Conference (EuRAD), 2013 European, 2013, pp. 33–36 [Online]. Available: http://ieeexplore.ieee.org/abstract/document/6689106/. [Accessed: 04-Sep-2017]

[17]   W.-D. Wirth and Institution of Electrical Engineers, Radar techniques using array antennas. London: Institution of Electrical Engineers, 2001.

[18]   R. C. Hansen, Phased array antennas, 2nd ed. Hoboken, N.J: Wiley, 2009.

[19]   M. A. Richards, J. A. Scheer, and W. A. Holm, Principles of modern radar. vol. 2, vol. 2,. Raleigh, N.C.: SciTech Pub., 2010.

[20]   C. A. Balanis, Antenna theory: analysis and design, 3rd ed. Hoboken, NJ: John Wiley, 2005.

[21]   M. A. Richards, J. Scheer, W. A. Holm, and W. L. Melvin, Eds., Principles of modern radar. Raleigh, NC: SciTech Pub, 2010.

[22]   J. Li and P. Stoica, Eds., MIMO radar signal processing. Hoboken, NJ: J. Wiley & Sons, 2009.

[23]   A. F. Yegulalp, 'Fast backprojection algorithm for synthetic aperture radar', in Radar Conference, 1999. The Record of the 1999 IEEE, 1999, pp. 60–65.

[24]   R. A. Kennedy, T. Abhayapala, D. B. Ward, and R. C. Williamson, 'Nearfield broadband frequency invariant beamforming', in Acoustics, Speech, and Signal Processing, 1996. ICASSP-96. Conference Proceedings., 1996 IEEE International Conference on, 1996, vol. 2, pp. 905–908 [Online]. Available: http://ieeexplore.ieee.org/xpls/abs_all.jsp?arnumber=543268. [Accessed: 11-Aug-2014]

[25]   R. A. Kennedy, D. B. Ward, and P. T. D. Abhayapala, 'Nearfield beamforming using

8

nearfield/farfield reciprocity', in *Acoustics, Speech, and Signal Processing, 1997. ICASSP-97., 1997 IEEE International Conference on*, 1997, vol. 5, pp. 3741–3744 [Online]. Available: http://ieeexplore.ieee.org/xpls/abs_all.jsp?arnumber=604683. [Accessed: 11-Aug-2014]

9